

# CMOS-fabricated ultraviolet light modulators using low-loss alumina piezo-optomechanical photonic circuits

Roman Shugayev<sup>1</sup>, Daniel Dominguez<sup>1</sup>, Andrew Leenheer<sup>1</sup>, Bethany Little<sup>1</sup>,  
Matthew N. H. Chow<sup>1</sup>, Nicholas Karl<sup>1</sup>, Matt Koppa<sup>1</sup>, Michael Gehl<sup>1</sup>, Yuan-Yu Jau<sup>1</sup>  
and Matt Eichenfield<sup>1\*</sup>

<sup>1</sup>*Sandia National Laboratories, 1515 Eubank Blvd, Albuquerque, NM, USA*

*\*eichenfield@arizona.edu*

We demonstrate a CMOS-foundry-fabricated piezo-optomechanical photonic integrated circuit platform for ultraviolet and blue wavelengths, using alumina waveguides that are strongly mechanically coupled to monolithically integrated aluminum nitride piezoelectric actuators. Low waveguide losses are measured down to at least 320 nm, where we achieve 1.6 dB/cm. This allows us to demonstrate broadband amplitude modulators based on piezoelectrically actuated MEMS cantilever phase-shifters down to 320 nm, with a high extinction ratio of 30 dB. We further demonstrate the versatility of the platform by designing and demonstrating a modulator that can work with high extinction and low loss at 320 nm and 420 nm, simultaneously, demonstrating control of multiple, disparate wavelengths in one device. We also demonstrate narrow-band resonant racetrack modulators with quality factors of  $4.7 \cdot 10^5$  and a tuning rate of 27.5 MHz/V. These results should open doors for a range of novel applications in UV photonics, quantum science, sensing and spectroscopy.

## Introduction

Integration of photonic devices with atomic quantum systems presents a new and exciting avenue for scalable quantum computing and sensing with atoms, ions, and other optically active qubits [1-5]. One of the most important criteria for scalability in this domain is simultaneously scalable photonic and electronic integration, which can most readily be achieved using CMOS foundry fabrication [6]. Trapped ions [7], neutral atoms [8-11], quantum dots [12], and diamond color centers [13] have all made various use of integration with on-chip photonic components. However, many of these quantum systems have indispensable optical transitions that require high-energy photons in the blue or ultraviolet (UV) wavelength range [14-19], and often need precise phase, amplitude, frequency, and polarization modulation. The demands on materials and fabrication to achieve ultra-low losses in the UV and near-UV are very high [20-23], and finding modulation mechanisms that meet the stringent requirements of high fidelity quantum gate operations while meeting the environmental constraints and scalability needs have made the development of truly VLSI solutions for this wavelength range remain elusive.

In addition to supporting scalable quantum architectures, applications for UV photonics exist for many important chemical and biological species which have a range of transitions at UV wavelengths, traditionally explored using UV-Vis spectroscopy [24-27]. Creating low-loss UV photonic material systems could allow *integrated* UV-Vis spectroscopy that would provide higher sensitivity, smaller volume, and lower cost spectroscopic testbeds [28]. As another example, in Raman spectroscopy, the signal scales as

the fourth power of the optical frequency of incident light, yielding distinct advantages for UV illumination compared to longer wavelength photons; this implies that integrated UV Raman systems could greatly increase measurement sensitivity and reduce minimal detectable limit [29-30]. Lab-on-chip chemical systems that can utilize UV and near-UV photons to catalyze and drive forward selected chemical reactions [31-33] could also be miniaturized and scaled to allow a large number of independent reactions to be driven and monitored simultaneously [34-35] for applications in parallel synthesis/drug discovery [36] and 3D tissue engineering [37]. For microfluidics, localized UV excitation can modulate the properties of the flow channel such as wettability and chromocapillary effects via *trans-cis* isomerization reactions helping to overcome the limitations of normally static microfluidic devices [38-39].

In this work, we have designed, fabricated, and characterized CMOS-compatible, cantilever-based piezoptomechanical photonic integrated circuits that can rapidly modulate UV and near-UV optical fields. As a demonstration of the wavelength versatility of the platform, we fabricate devices working at 320 nm and 420 nm on the same chip *and* individual devices that can perform locally broadband modulation of both these wavelengths, simultaneously. These particular wavelengths were chosen due to their use for important transitions in cesium, strontium, and rubidium, which are used to produce entangling gates in neutral atom quantum computing systems. Specifically, these wavelengths support the  $6S_{1/2} \rightarrow -NP_{3/2}$  and  $5^3P_0 \rightarrow N^3S_1$  single-photon transitions to Rydberg state with principal quantum number,  $N$ , at 319 nm and 317 nm in cesium and strontium, respectively, and the  $5S_{1/2} \rightarrow 6P_{3/2}$  transition at 420 nm, used for two-photon Rydberg control in rubidium (when combined with 1013 nm photons) [40-43]. However, as discussed above, the application space spanned by the demonstrations herein is quite large. We demonstrate low UV propagation losses in waveguide based devices, with 1.6 dB/cm loss down to as low as 320 nm, and we use these waveguides to demonstrate Mach-Zehnder modulators with high extinction ratios in two bands, simultaneously: 30 dB at 420 nm and 14 dB at 320 nm. We also demonstrate high-quality-factor UV resonators ( $\sim 4.7 \cdot 10^5$  at 320 nm), as well as fast resonator tuning rates (27.5 MHz/V).

### System and fabrication description

Broadband amplitude modulators are preferable to narrow-band, resonant modulators when the light being modulated must be at a very specific wavelength, such as when addressing atomic transitions. Even the most advanced photonic VLSI fabrication will generally result in a large spread of resonance frequencies across a wafer [44], requiring substantial post-fabrication tuning[45-46] or trimming[47-48]. Mach-Zehnder interferometer (MZI) modulators are one of the most common implementation of broadband amplitude modulators at telecommunications wavelengths [49-50]. The potential drawback of MZI modulators is that larger devices can be required to achieve sufficient phase shift compared to resonant devices. While several ways exist to achieve the MZI internal phase shift that drives amplitude modulation, such as the electro-optic and magneto-optic effect [51-52], in this work we use the optomechanical phase shift induced on integrated MEMS cantilevers similar to those recently demonstrated for visible-light quantum photonics [53-54]. The footprint of these devices are compatible with many conceptions of scalable photonic architectures for quantum computing[55], and their modulation bandwidths have been demonstrated at tens[54,71] and even hundreds[53] of megahertz, which is sufficient for most atomic transitions. Importantly, the accuracy and repeatability of piezoptomechanical MZI modulators using AlN at room temperature has been demonstrated to be compatible

with high-fidelity single-qubit gates in trapped ions[56], motivating their exploration for more complex gate operations such as entangling two-qubit gates in trapped neutral atoms[57].

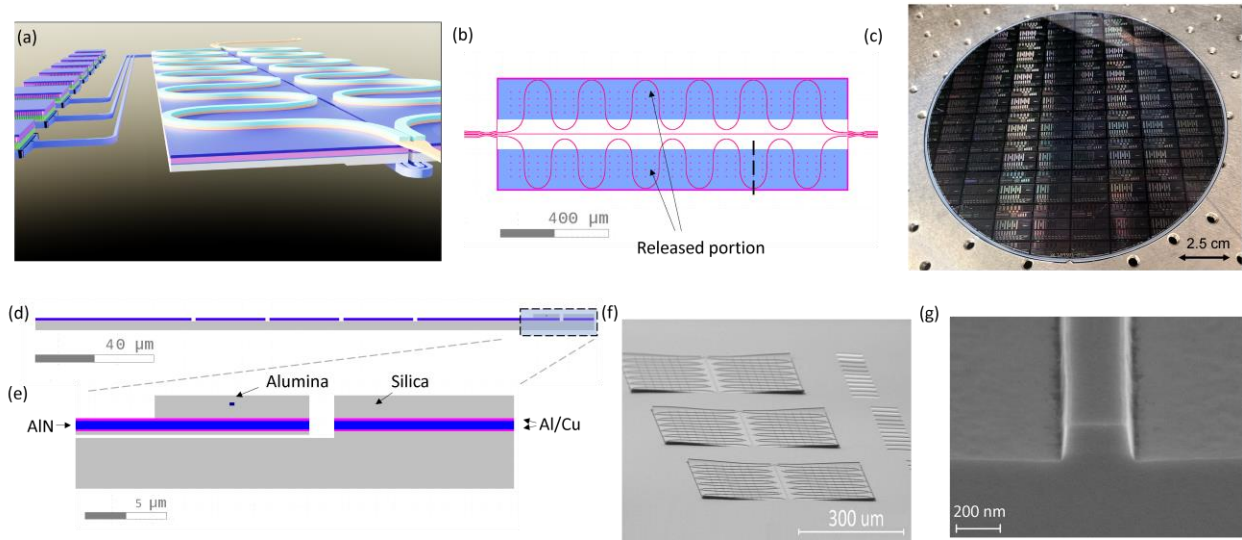


Figure 1. (a) Conceptual 3D drawing of the CMZI device. Vertical dimension is enhanced 10X for clarity. (b) Top layout view of the device highlighting the released portion. Cross section line is shown in dots. (c) Top view of the fabricated wafer. (d) Cross-section of a CMZI device. (e) Zoom of the highlighted portion. (f) Tilted SEM image of fabricated CMZI devices. (g) Representative SEM cross section of the fabricated alumina waveguide.

Our integrated differential Mach-Zehnder interferometer (MZI) uses alumina waveguides that meander along piezoelectrically actuated cantilevers, as shown in Figure 1. The cantilever is fabricated using similar processes to ref. [53-54], but the silicon nitride waveguide was replaced by 200-nm-thick  $\text{Al}_2\text{O}_3$  deposited using atomic layer deposition (ALD). The cantilever is released by removing a patterned amorphous silicon layer underneath the overhang using  $\text{XeF}_2$  (Figure 1(d,e)). All processing was performed in a volume CMOS foundry at Sandia National Labs on 200 mm wafers (Figure 1(c)); the entire process is also back-end-of-line CMOS compatible and could be fabricated directly on top of and connected to CMOS application-specific integrated circuits (ASICs)[58-59].

Piezoelectric actuation is provided by an aluminum nitride (AlN) thin-film layer positioned between AlCu metallic films (Figure 1(a)) that are individually routed vertically through the device and an independent metal routing layer, allowing independent potentials to be applied to the top and bottom of the AlN film and be routed to the chip edges in dense circuits using multi-level metal routing. The electrical connection to the device was made through AlCu pads on the surface of the chip (Figures 1 (a), 5 (a)) in a GSGS configuration that allowed for independent bias control of the two MZI arms with a single probe. The fields are applied parallel to the C-axis of the polycrystalline AlN, and the strain that provides modulation is in-plane normal strain, thus governed by the  $d_{31}$  piezoelectric coefficient [60-61]. Vertical asymmetry in geometry of the actuating patch results in linear Euler-Bernoulli strain along the cantilever thickness which in turn produces bending action, in addition to the elongation and contraction that predominantly produces modulation.

Equal but opposite voltages were applied independently to each arm, maximizing the total produced phase difference, though we have also demonstrated the ability to do this using a single potential that is

applied oppositely to both arms by switching which electrode is ground or signal in the arms[53]. The response to the applied voltage has two contributions. First, there exists a photoelastic modulation of the refractive index induced by strain and described in the case of, for instance,  $n_1$  component as [62]

$$\Delta n_1 = -\frac{1}{2}n^3(p_{11}S_1 + p_{12}S_2 + p_{12}S_3) \quad (1)$$

Where  $p_{ij}$  is a Voigt-contracted photoelastic coefficient,  $S_j$  is one the Voigt-contracted normal strain tensor components, and  $n$  is the (isotropic) refractive index. Figure 2 (d) shows the resulting photoelastic change in refractive index tensor along the waveguide when taking a path along a single loop of the CMZI device. For these simulations we have used published photoelastic coefficients for SiO<sub>2</sub> and alumina [63-64].

Second, there is a phase change due to effective path-length change of the waveguide modes. The path-length change can be found by integrating the gradient of displacement,  $\nabla \mathbf{u}$ , over the full waveguide path [54] according to the formula

$$\Delta L = \int_c ds \hat{s} \cdot \nabla \mathbf{u} \cdot \hat{s} \quad (2)$$

where  $\hat{s}$  is the unit vector along the integration path (Figure 2(b)). Because of the weak index contrast of the two waveguide materials, the optomechanical moving boundary effect is largely irrelevant to changes in the propagation constant of the waveguide under applied strain[65].

The devices were modeled using multi-physics finite element software (COMSOL) to first optimize and then verify their performance. Our simulation results show that approximately 78% of the total modulation is due to path length change (Figure 2 (c)), and 22% is due to photoelastic index modulation (Figure 2 (d)). Importantly, the model predicts that the path-length and photoelastic modulation effects add constructively, as opposed to partially canceling each other.

The directional coupler for the MZI was designed using a 2D model of the waveguide cross-section to solve for the symmetric/antisymmetric supermodes and use their derived propagation constants to calculate the beat length of the coupler. In the simulation we have used in-house ellipsometry alumina measurements (Supplemental, Figure S2) and silica results from the literature [66]. Modeling results for power at the output power positioned on the same side of the coupler as the input port are shown on Figure 3 (a). The combination of wide single-mode operation of the waveguides, large material dispersion of alumina, and the increase in the evanescent tail coupling with increasing wavelength allows us to design 50/50 couplers that work at very disparate wavelengths in the same device. This could be useful for multi-species trapped atom systems that require many wavelengths to be operated on simultaneously[67-70] and demonstrates the versatility of the platform. Based on the modeling, the ~50/50 splitting point occurs at a similar coupler length ( $L_c \approx 17.2 \text{ um}$ ) for both 320 nm and 420 nm which corresponds to  $\frac{1}{2}\pi$  beat frequency phase shift at 320 nm and  $\frac{3}{2}\pi$  phase shift at 420 nm.

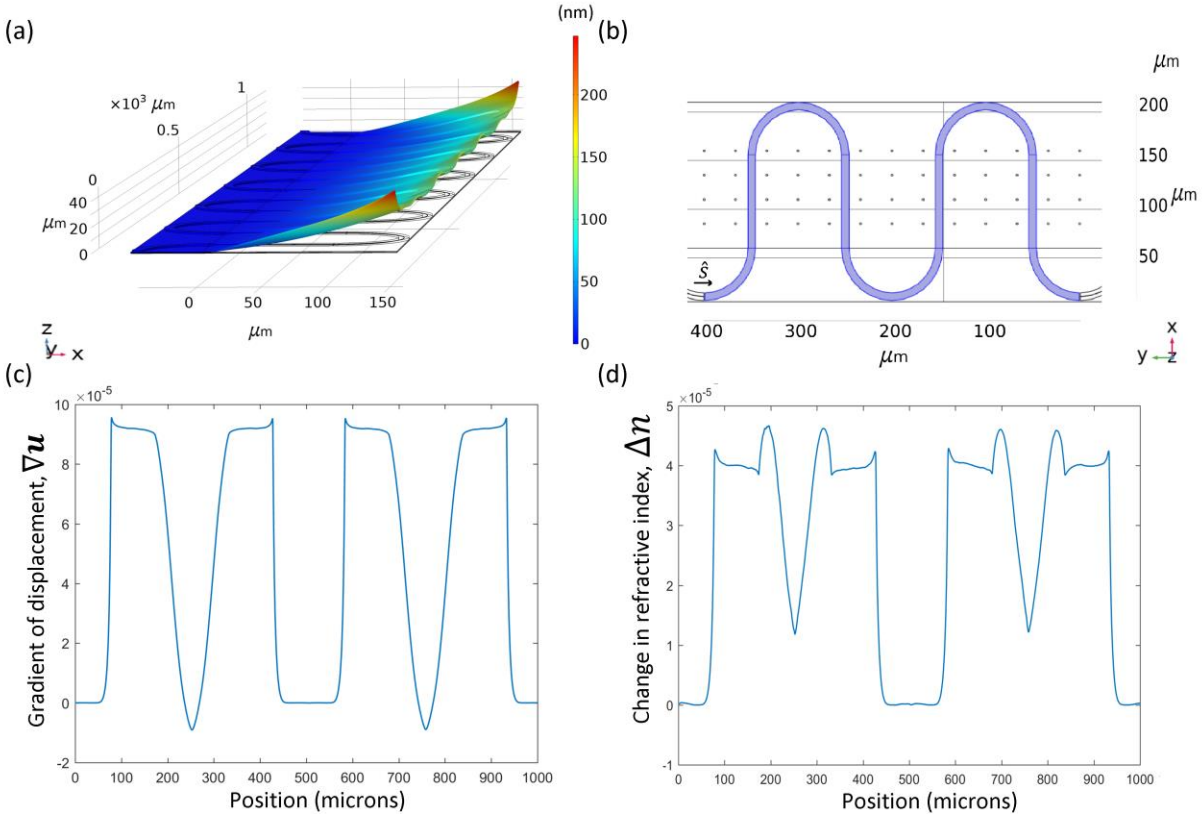


Figure 2. (a) COMSOL Multiphysics simulations of CMZI mechanical deflection for -20 V applied voltage. (b) Top view of the optical path used in photoelastic and path change plots. (c) Gradient of displacement taken along the waveguide length. (d) Photoelastic change in refractive index along the waveguide length.

### Experimental characterization

The fabricated devices were tested using lens-tapered fibers (LTFs) to edge-couple the UV laser light onto the chip. The edge-coupling incorporated an inverse tapered waveguide with 0.5  $\mu\text{m}$  waveguide facet width to achieve the most efficient mode matching of the waveguide mode at the taper end to the free-space mode at the LTF's focus. Devices on the die were routed with input and output waveguides orthogonally oriented to prevent stray laser light coupling directly across the chip to the photodetector. The uniformity of deflection profiles of fabricated cantilever devices from SEM images (Figure 1(f)) suggested high degree of reproducibility.

320 nm laser light was produced via a free-space, frequency doubling source that converted a 640 nm solid state laser (UnikLasers) light to 320 nm using a doubling cavity (COHERENT MBD-200). Transmission measurements were performed at both 320 nm and 420 nm wavelengths in the same cantilever MZI device ( $L_c \approx 15 \mu\text{m}$ ). In this test, the voltage was linearly ramped from -20 to 20 V (Figure 3 (b)). As desired and designed via our model (see above), the single device achieves 30 dB of extinction at 420 nm and 14 dB at 320 nm. The extinction ratios could be further improved by including more finely varied designs of the direction coupler in the future. The difference in experimental vs modeling results for 50/50 coupler splitting are likely due to fabrication tolerances and errors in the modeled optical constants for the waveguide and clad materials. For example, the gap between the waveguides in the coupling region

(Supplemental, Figure S3) depends critically on local lithography and etch effects which modify the resulting geometry compared to the model. We also observe a difference in the voltage at which the device produces maximum extinction for each of the two wavelengths; this is likely due to the difference in effective path length between two arms of the MZI due to fabrication and/or built-in stress. From the figures we can observe that it takes only  $\sim 12.5$  Volts (at 320 nm) to travel from the transmission maximum to minimum which should be beneficial for low-power/low-voltage integrated electronics operation. We derive the  $V_{\pi}$  estimate for the cantilever device as  $V_{\pi} \approx 28$  V and corresponding  $V_{\pi} \cdot L = 5.9$  V  $\cdot$  cm.

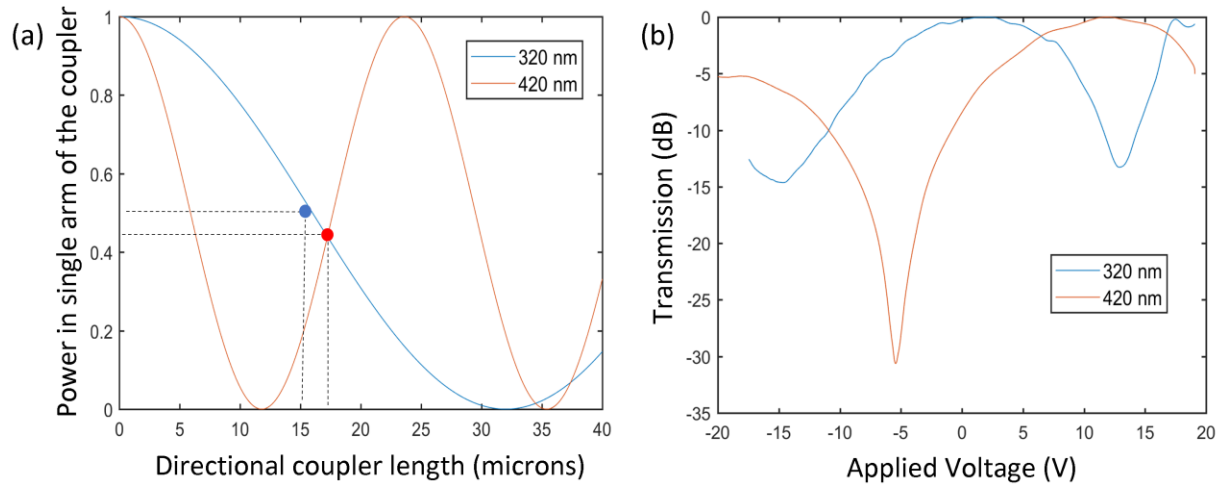


Figure 3. (a) Simulated results for normalized directional coupler transmission vs. coupler length. Blue dot indicates the experimentally measured 50/50 point for directional coupler both at 320 and 420 nm and red dot indicates corresponding modeling results. Transmission vs. applied voltage on CMZI device at 420 nm and 320 nm (b).

One of the most important modulator metrics for quantum information processing applications is the modulation or switching rate. We characterize this in two ways. First, we do S-parameter testing that looks at the response to sinusoidal excitations of varying frequencies, and, second, we perform transient rectangle-wave tests which emulate realistic modulation of device transmission in a switching application. In the first case, the device was excited by 420 nm laser light, and its transmission was measured by the fast detector. 10 mW of RF power was applied by a vector network analyzer to the device via the GSGS probes. The received optical transmission was routed to the detector port of the network analyzer to produce the combined S21 measurement. The intermediate frequency (IF) bandwidth setting was 200 Hz, and we show 10 averages of the frequency sweep in figure 4(a,b).

Figure 4 (a,b) shows the results for the magnitude S21 parameter measurements with and without laser illumination, to distinguish device response from the spurious noise and intrinsic detector responsivity. Figure 4a shows the frequency response is relatively flat until  $\sim 6$  MHz, after which it experiences several smaller resonances and drops  $\sim 4$  dB in the interval 4-10 MHz. Figure 4b shows that there is a rapid roll-off at frequencies above the 10 MHz detector bandwidth. At higher frequencies we observe high-Q, resonances, which can be attributed to resonant excitation of the mechanical eigenmodes of the CMZI structure (Figure 4 (b), insert).

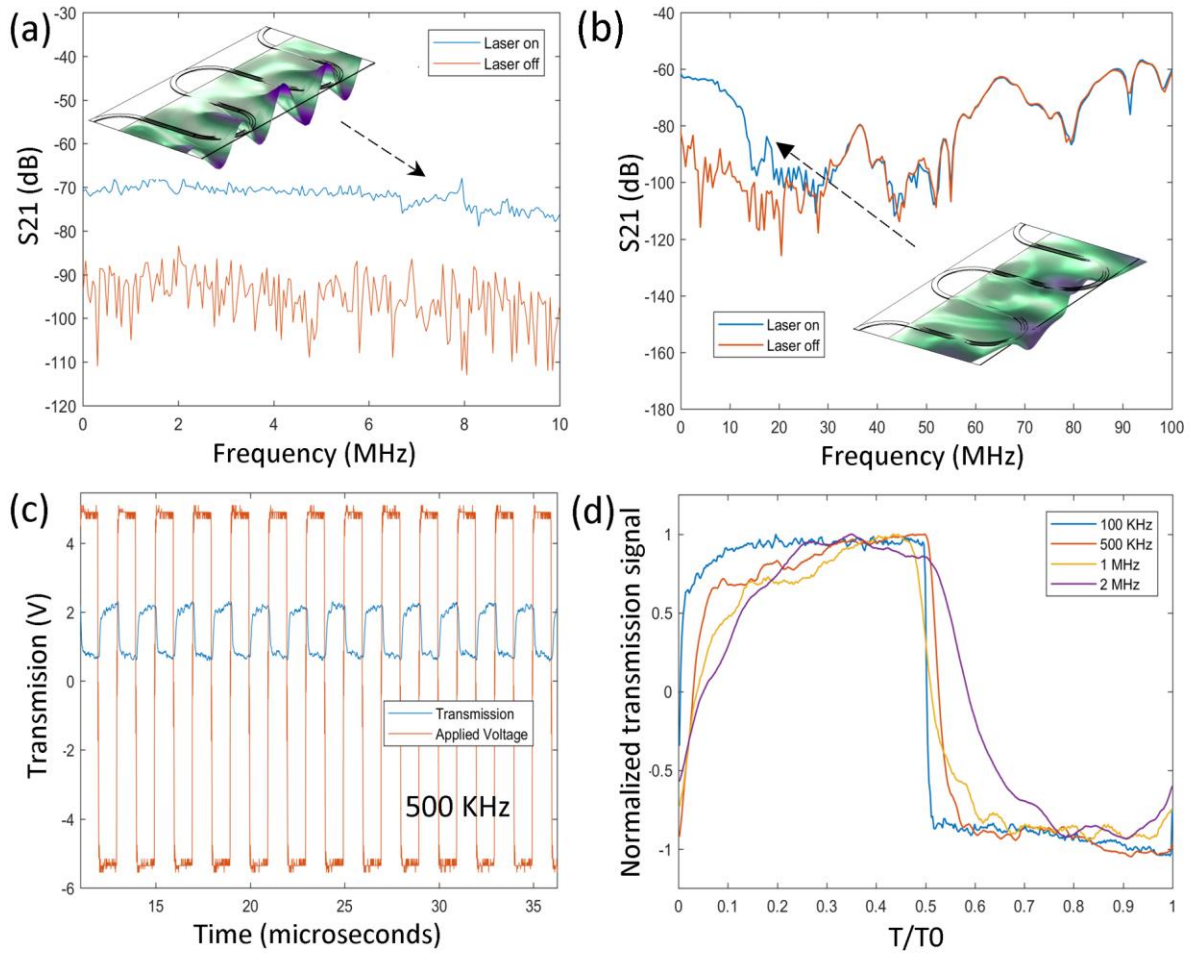


Figure 4. Network analyzer characterization of the CMZI modulator. S21 scans up to 10 MHz (a) and 100 MHz (b). The network analyzer dark background signal is shown for comparison. Inserts: COMSOL simulated mode profiles for 6.4 MHz and 17.7 MHz resonant mode. (c) Square wave response of the CMZI device at 500 kHz. (d) Single pulse averaged response to a square wave excitation at different frequencies; axes are normalized for magnitude and period.

Figures 4(c,d) show the result of a  $10 V_{pp}$  square wave from an arbitrary waveform generator applied to the device while varying the signal frequency (Figure 4(c,d)). The time-domain transmission signal was recorded using a sampling oscilloscope and, in the case of Figure 4 (d), averaged over 50 cycles. Figure 4d shows the results of increasing square-wave frequency drives, with the finite response time of the overall system becoming apparent as the drive frequency approaches  $\sim 1$  MHz. The measured response time can be attributed to both the finite bandwidth of the avalanche photodiode detector used in the measurement as well as the presence of the resonant cantilever modes at harmonics of the square wave.

We measured the propagation losses for our platform at 320 nm using a piezo-optomechanical racetrack resonator with a roundtrip length of  $L = 1$  cm, as shown in Figure 5 (a). The racetrack device was also monolithically coupled to the underlying piezoelectric strain actuator, and the cross-section of the active



region (Figure 5(b)) was the same as in our previously demonstrated strain tuning device [53]. Reconfigurable, low-loss photonic devices operating in the UV are challenging to achieve due to various loss mechanisms specific to the UV. For example, at UV wavelengths, waveguide sidewall roughness and absorptive optical transmissions due to surface or bulk chemical states [71-73] can become more detrimental than at visible or infrared wavelengths. Here we report, to the best of our knowledge, a first demonstration of low-loss operation of a piezo-optomechanical reconfigurable resonant filter at 320 nm.

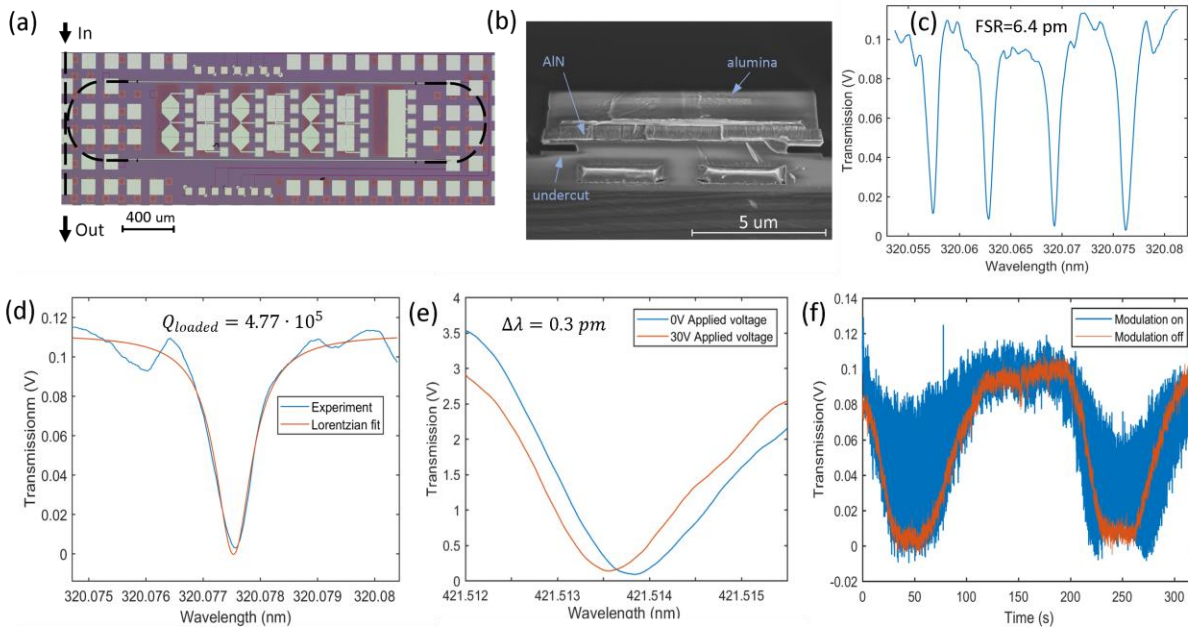


Figure 5. Tunable racetrack resonator. (a) top-view high resolution optical image of the racetrack resonator die; dummy metal fill features and unrelated test structures are also visible. Contour of the optical waveguide is shown in dotted lines. (b) SEM cross section of the layer stack, showing a fabricated racetrack resonator device. (c) Effective wavelength sweep showing multiple transmission fringes. (d) Lorentzian fit of a single peak. (e) Single fringe shift resulting from applying of the DC voltage. (f) 320 nm thermal sweep of the device with and without applied 10 Hz sinusoidal voltage.

A temperature sweep was performed by attaching the die to the planar ohmic heater with adhesive tape and applying a slow voltage ramp to the heater while measuring 320 nm laser transmission through the device. The use of thermal sweep was motivated by the fixed wavelength of the laser and also as it served as an additional tuning knob for control of the resonator that provided significantly more tuning than the piezoelectric tuning, alone. In this case, the thermo-optic effect, which acts to modify the refractive index, allows us to obtain effective spectral transmission data. The heater's slow triangular waveform voltage sweep frequency was set at 0.0025 Hz with the amplitude  $20 V_{peak}$ . The resonator was modeled via FEM to obtain a free spectral range of 6.4 picometers, using the as-drawn device geometry and measured material parameters, including the film thicknesses and indices measured by ellipsometry and waveguide and core width measured by calibrated SEM. The modeled FSR was then used to set the wavelength scale for the obtained spectral plots in the transmission vs temperature, which was in-turn used to fit the transmission to a Lorentzian and extract the quality factor. The quality factor of the resonator was



obtained from the linewidth parameter of a Lorentzian fit (Figure 5 (d)) to be  $Q_{loaded} = 4.77 \cdot 10^5$ . Coupled mode theory allowed the transmission of the cavity and loaded quality factor to be used to obtain a quality factor  $Q_{int} = (9.6 \pm 1) \cdot 10^5$ , with the uncertainty coming from the nearly critically coupled resonance having ambiguity between being under- and over-coupled. The waveguide loss corresponding to this quality factor is

$$\alpha = \frac{2\pi n_g}{Q_{int}\lambda_0} \quad (3)$$

where  $n_g$  is the group index of the propagating mode (Supplemental, S4), which results in a propagation loss estimate of  $\alpha = 1.6$  dB/cm at  $\lambda = 320$  nm. Therefore, the previously described cantilever MZI device, which uses the same waveguide cross-section, would have a propagation loss of 0.33 dB over its length of 0.21 cm, if bending losses were negligible. At 420 nm we estimate the waveguide loss using similar alumina waveguides with linearly increasing length (Figure S6), from which we estimate a loss of 0.86 dB/cm.

The same active racetrack resonator was also used to measure the resonator tunability both at 420 and 320 nm. Figure 5(e) shows the results of the 420 nm TOPTICA laser wavelength sweep with and without the application of DC voltage to the piezoelectric. We observe a clear shift corresponding to photoelastically induced refractive index change of the alumina resonator. By locking the laser to the resonance and using a wavelength meter to measure the resulting laser wavelength vs voltage applied to the resonator, we measure 25.9 MHz/V. Finally, we have performed a thermal scan at 320 nm while applying sinusoidal voltage to the piezoelectric under the resonator device (Figure 5(f)). Analyzing the maximum transmission change corresponding to the locations of the fringes revealed a tunability of about 27.5 MHz/V. As a fraction of FSR the tuning range of  $\pm 100$  V corresponds to  $\approx 32\%$  of the FSR.

## Discussion

We demonstrate the first realization of piezoelectrically tunable photonics in the UV frequency band using aluminum nitride actuators coupled to alumina waveguides. Improvements in the directional couplers and cascading devices could be used to improve the extinction ratio. The relatively small size of fabricated devices compared to alternative implementations [53] permits a high density of integration for classical and quantum on-chip light manipulation. The phase modulation devices comprising a single suspended cantilever can be put in series with cantilever MZIs for full control of the amplitude and phase of the beam.

Additional benefits for extinction ratio and wavelength range would result from tunable directional couplers which could be envisioned with the same undercut/active control method or temperature control approaches [74]. Size reduction can be improved with optimized designs targeting more efficient piezoelectric transduction, such as material selection[75], optimization of the film thicknesses[76], etc. Further improvement can potentially be brought by systematic and/or inverse design search for waveguiding routing patterns with maximized path length change and photoelastic refractive index change [77-78]. The tunability could potentially be further improved by optimizing the cross-section geometry of the undercut section of the device (Figure 5(b)) such as increasing the width of the undercut region.

For future uses of the resonator device as a spectrometer or chemical reactor the top cladding can be etched down[79-80] after which surface adsorbed molecule transmission spectrum can be monitored and selected transitions can be excited through the evanescent tail coupling. Further integration with microfluidic devices can be implemented for better experiment control and high throughput applications [81].

Previously, we have demonstrated cryogenic operation of the same platform used in this paper with SiN waveguides [53, 80, 82]. Our current devices were fabricated with alumina which has been shown to have reduced cryogenic transmission losses in IR/THz range [83-84]. Single crystal  $\text{Al}_2\text{O}_3$  optical devices have also been widely used at cryogenic temperatures in both visible and UV range [85-88]. Therefore, we expect the devices demonstrated in this work to be operational at cryogenic temperatures as well for current and future quantum applications in UV regime.

## Conclusion

In conclusion we have demonstrated photonic integrated circuit devices in technologically and scientifically important blue and UV range using piezo-optomechanical modulation of alumina waveguides. The cantilevered-MZI (CMZI) devices operated at both 320 and 420 nm wavelengths, have a compact size, a high isolation ratio, and allow for relatively fast switching. The tunable racetrack resonators with small FSR provide an alternate device architecture to cover a wide range of the UV spectrum when combining the fast piezo tuning with slower thermal tuning. The blue and UV operation of these active, tunable devices open doors for many new and exciting applications of UV integrated photonics. Overall, the demonstrated platform presents significant step forward towards wider applicability and technological importance of UV photonics.

## Methods

The 320 nm power before the edge coupling used in the optical PIC tests was 0.8 mW continuous wave. For quasistatic transmission vs. applied voltage tests and thermal tests, we used a high gain Thorlabs detector (PDF10A2). For high-speed AC studies, a fast avalanche photodetector (APD410A2) with 10 MHz bandwidth was utilized. Also for the AC studies we've used Agilent E5071C 8.5 GHz network analyzer, AFG3022C 250 Ms/s 25MHz arbitrary waveform generator and the Keysight DSOX1202A 2Gs/s 70MHz digital storage oscilloscope.

## Acknowledgments

This work is supported by Sandia Laboratory Directed Research and Development (LDRD) and Quantum Systems through Entangled Science and Engineering (Q-SEnSE) funded by National Science Foundation Quantum Leap Challenge Institute (NSF QLCI). Sandia National Laboratories is a multimission laboratory managed and operated by National Technology & Engineering Solutions of Sandia, LLC, a wholly owned subsidiary of Honeywell International Inc., for the U.S. Department of Energy's National Nuclear Security Administration under contract DENA0003525. This paper describes objective technical results and analysis. Any subjective views or opinions that might be expressed in the paper do not necessarily represent the views of the U.S. Department of Energy or the United States Government. This material is

based upon work supported by the U.S. Department of Energy, Office of Science, National Quantum Information Science Research Centers, Quantum Systems Accelerator. Additional support is acknowledged from [other agencies]. M.E. performed this work, in part, at the Center for Integrated Nanotechnologies, an Office of Science User Facility operated for the U.S. Department of Energy Office of Science.

## References

1. Morgado, M. and Whitlock, S., 2021. Quantum simulation and computing with Rydberg-interacting qubits. *AVS Quantum Science*, 3(2)
2. Atom Computing “Quantum startup Atom Computing first to exceed 1,000 qubits” Press Release (2023)
3. Brown, K.R., Kim, J. and Monroe, C., 2016. Co-designing a scalable quantum computer with trapped atomic ions. *npj Quantum Information*, 2(1), pp.1-10
4. Wan, N.H., Lu, T.J., Chen, K.C., Walsh, M.P., Trusheim, M.E., De Santis, L., Bersin, E.A., Harris, I.B., Mouradian, S.L., Christen, I.R. and Bielejec, E.S., 2020. Large-scale integration of artificial atoms in hybrid photonic circuits. *Nature*, 583(7815)
5. Yan, X., Gitt, S., Lin, B., Witt, D., Abdolahi, M., Afifi, A., Azem, A., Darcie, A., Wu, J., Awan, K. and Mitchell, M., 2021. Silicon photonic quantum computing with spin qubits. *APL Photonics*, 6(7)
6. Elshaari, A.W., Pernice, W., Srinivasan, K., Benson, O. and Zwiller, V., 2020. Hybrid integrated quantum photonic circuits. *Nature photonics*, 14(5), pp.285-298.
7. Ivory, M., Setzer, W.J., Karl, N., McGuinness, H., DeRose, C., Blain, M., Stick, D., Gehl, M. and Parazzoli, L.P., 2021. Integrated optical addressing of a trapped ytterbium ion. *Physical Review X*, 11(4), p.041033
8. Chauhan, N., Bose, D., Puckett, M., Moreira, R., Nelson, K. and Blumenthal, D.J., 2019, May. Photonic integrated Si 3 N 4 ultra-large-area grating waveguide MOT interface for 3D atomic clock laser cooling. In *2019 Conference on Lasers and Electro-Optics (CLEO)* (pp. 1-2). IEEE.
9. Ropp, C., Zhu, W., Yulaev, A., Westly, D., Simelgor, G., Rakholia, A., Lunden, W., Sheredy, D., Boyd, M.M., Papp, S. and Agrawal, A., 2023. Integrating planar photonics for multi-beam generation and atomic clock packaging on chip. *Light: Science & Applications*, 12(1), p.83
10. Lee, J., J. A. Grover, L. A. Orozco, and S. L. Rolston. "Sub-Doppler cooling of neutral atoms in a grating magneto-optical trap." *JOSA B* 30, no. 11 (2013): 2869-2874.
11. Lee, Jongmin, Roger Ding, Justin Christensen, Randy R. Rosenthal, Aaron Ison, Daniel P. Gillund, David Bossert et al. "A compact cold-atom interferometer with a high data-rate grating magneto-optical trap and a photonic-integrated-circuit-compatible laser system." *Nature Communications* 13, no. 1 (2022): 5131.
12. Hepp, S., Jetter, M., Portalupi, S.L. and Michler, P., 2019. Semiconductor quantum dots for integrated quantum photonics. *Advanced Quantum Technologies*, 2(9), p.1900020

13. Lenzini, F., Gruhler, N., Walter, N. and Pernice, W.H., 2018. Diamond as a platform for integrated quantum photonics. *Advanced Quantum Technologies*, 1(3), p.1800061
14. Bernien, Hannes, Sylvain Schwartz, Alexander Keesling, Harry Levine, Ahmed Omran, Hannes Pichler, Soonwon Choi et al. "Probing many-body dynamics on a 51-atom quantum simulator." *Nature* 551, no. 7682 (2017): 579-584
15. Engel, Felix, Thomas Dieterle, Thomas Schmid, Christian Tomschitz, Christian Veit, Nicolas Zuber, Robert Löw, Tilman Pfau, and Florian Meinert. "Observation of Rydberg blockade induced by a single ion." *Physical Review Letters* 121, no. 19 (2018): 193401.
16. Saßmannshausen, Heiner, Frédéric Merkt, and Johannes Deiglmayr. "High-resolution spectroscopy of Rydberg states in an ultracold cesium gas." *Physical Review A* 87, no. 3 (2013): 032519.
17. Keating, Tyler, Kritika Goyal, Yuan-Yu Jau, Grant W. Biedermann, Andrew J. Landahl, and Ivan H. Deutsch. "Adiabatic quantum computation with Rydberg-dressed atoms." *Physical Review A* 87, no. 5 (2013): 052314.
18. Ebadi, Sepehr, Tout T. Wang, Harry Levine, Alexander Keesling, Giulia Semeghini, Ahmed Omran, Dolev Bluvstein et al. "Quantum phases of matter on a 256-atom programmable quantum simulator." *Nature* 595, no. 7866 (2021): 227-23
19. Monroe, C. and Kim, J., 2013. Scaling the ion trap quantum processor. *Science*, 339(6124), pp.1164-1169
20. Blumenthal, Daniel J. "Photonic integration for UV to IR applications." *APL Photonics* 5, no. 2 (2020).
21. West, Gavin N., William Loh, Dave Kharas, Cheryl Sorace-Agaskar, Karan K. Mehta, Jeremy Sage, John Chiaverini, and Rajeev J. Ram. "Low-loss integrated photonics for the blue and ultraviolet regime." *Apl Photonics* 4, no. 2 (2019)
22. Huang, Chen, Haochen Zhang, and Haiding Sun. "Ultraviolet optoelectronic devices based on AlGaIn-SiC platform: Towards monolithic photonics integration system." *Nano energy* 77 (2020): 105149.
23. Moody, Galan, Volker J. Sorger, Daniel J. Blumenthal, Paul W. Juodawlkis, William Loh, Cheryl Sorace-Agaskar, Alex E. Jones et al. "2022 Roadmap on integrated quantum photonics." *Journal of Physics: Photonics* 4, no. 1 (2022): 012501
24. Schmid, F.X., 2001. Biological macromolecules: UV-visible spectrophotometry. e LS.
25. Perkampus, Heinz-Helmut. *UV-VIS Spectroscopy and its Applications*. Springer Science & Business Media, 2013.
26. Picollo, Marcello, Maurizio Aceto, and Tatiana Vitorino. "UV-Vis spectroscopy." *Physical sciences reviews* 4, no. 4 (2018): 20180008.
27. Verma, Govinda, and Manish Mishra. "Development and optimization of UV-Vis spectroscopy-a review." *World J. Pharm. Res* 7, no. 11 (2018): 1170-1180.
28. Leitis, A., Tittl, A., Liu, M., Lee, B.H., Gu, M.B., Kivshar, Y.S. and Altug, H., 2019. Angle-multiplexed all-dielectric metasurfaces for broadband molecular fingerprint retrieval. *Science advances*, 5(5), p.eaaw2871.
29. Smith, Ewen, and Geoffrey Dent. *Modern Raman spectroscopy: a practical approach*. John Wiley & Sons, 2019
30. Nagli, L., M. Gaft, Y. Flegler, and M. Rosenbluh. "Absolute Raman cross-sections of some explosives: Trend to UV." *Optical Materials* 30, no. 11 (2008): 1747-1754

31. Guan, Y., Wen, H., Cui, K., Wang, Q., Gao, W., Cai, Y., Cheng, Z., Pei, Q., Li, Z., Cao, H. and He, T., 2024. Light-driven ammonia synthesis under mild conditions using lithium hydride. *Nature Chemistry*, pp.1-7.
32. Goti, Giulio, Kavyasree Manal, Jayaraman Sivaguru, and Luca Dell'Amico. "The impact of UV light on synthetic photochemistry and photocatalysis." *Nature Chemistry* (2024): 1-9.
33. Geng, Zhi, Yu Zhang, Xing Yuan, Mingxin Huo, Yahui Zhao, Ying Lu, and Yue Qiu. "Incorporation of Cu<sub>2</sub>O nanocrystals into TiO<sub>2</sub> photonic crystal for enhanced UV–visible light driven photocatalysis." *Journal of Alloys and Compounds* 644 (2015): 734-741.
34. Ahsan, S.S., Gumus, A. and Erickson, D., 2013. Redox mediated photocatalytic water-splitting in optofluidic microreactors. *Lab on a Chip*, 13(3), pp.409-414
35. Pimparkar, K., Yen, B., Goodell, J.R., Martin, V.I., Lee, W.H., Porco Jr, J.A., Beeler, A.B. and Jensen, K.F., 2011. Development of a photochemical microfluidics platform. *Journal of Flow Chemistry*, 1(2), pp.53-55.
36. Schneider, G., 2018. Automating drug discovery. *Nature reviews drug discovery*, 17(2), pp.97-113.
37. Rosenfeld, A., Göckler, T., Kuzina, M., Reischl, M., Schepers, U. and Levkin, P.A., 2021. Designing Inherently Photodegradable Cell-Adhesive Hydrogels for 3D Cell Culture. *Advanced healthcare materials*, 10(16), p.2100632.
38. Baigl, D., 2012. Photo-actuation of liquids for light-driven microfluidics: state of the art and perspectives. *Lab on a Chip*, 12(19), pp.3637-3653
39. Ichimura, Kunihiro, Sang-Keun Oh, and Masaru Nakagawa. "Light-driven motion of liquids on a photoresponsive surface." *Science* 288, no. 5471 (2000): 1624-1626.
40. Madjarov, Ivaylo S., Jacob P. Covey, Adam L. Shaw, Joonhee Choi, Anant Kale, Alexandre Cooper, Hannes Pichler, Vladimir Schkolnik, Jason R. Williams, and Manuel Endres. "High-fidelity entanglement and detection of alkaline-earth Rydberg atoms." *Nature Physics* 16, no. 8 (2020): 857-861.
41. Manetsch, Hannah J., Gyohei Nomura, Elie Bataille, Kon H. Leung, Xudong Lv, and Manuel Endres. "A tweezer array with 6100 highly coherent atomic qubits." arXiv preprint arXiv:2403.12021 (2024).
42. Hankin, A. M., Y-Y. Jau, L. P. Parazzoli, C. W. Chou, D. J. Armstrong, A. J. Landahl, and G. W. Biedermann. "Two-atom Rydberg blockade using direct  $6S$  to  $nP$  excitation." *Physical Review A* 89, no. 3 (2014): 033416
43. Bluvstein, Dolev, Harry Levine, Giulia Semeghini, Tout T. Wang, Sepehr Ebadi, Marcin Kalinowski, Alexander Keesling et al. "A quantum processor based on coherent transport of entangled atom arrays." *Nature* 604, no. 7906 (2022): 451-456.
44. Chrostowski, Lukas, et al. "Impact of fabrication non-uniformity on chip-scale silicon photonic integrated circuits." *Optical Fiber Communication Conference. Optica Publishing Group*, 2014.
45. Wu, Xi, et al. "High-Q microresonators integrated with microheaters on a 3C-SiC-on-insulator platform." *Optics letters* 44.20 (2019): 4941-4944.
46. Abel, Stefan, et al. "A hybrid barium titanate–silicon photonics platform for ultraefficient electro-optic tuning." *Journal of Lightwave Technology* 34.8 (2016): 1688-1693.

47. Menssen, Adrian J., Artur Hermans, Ian Christen, Thomas Propson, Chao Li, Andrew J. Leenheer, Matthew Zimmermann et al. "Scalable photonic integrated circuits for high-fidelity light control." *Optica* 10, no. 10 (2023): 1366-1372
48. Farmakidis, Nikolaos, et al. "Scalable high-precision trimming of photonic resonances by polymer exposure to energetic beams." *Nano Letters* 23.11 (2023): 4800-4806.
49. Miller, David AB. "Perfect optics with imperfect components." *Optica* 2, no. 8 (2015): 747-750. .
50. Harris, Nicholas C., Darius Bunandar, Mihir Pant, Greg R. Steinbrecher, Jacob Mower, Mihika Prabhu, Tom Baehr-Jones, Michael Hochberg, and Dirk Englund. "Large-scale quantum photonic circuits in silicon." *Nanophotonics* 5, no. 3 (2016): 456-468.
51. Sinatkas, Georgios, Thomas Christopoulos, Odysseas Tsilipakos, and Emmanouil E. Kriezis. "Electro-optic modulation in integrated photonics." *Journal of Applied Physics* 130, no. 1 (2021).
52. Pintus P, Ranzani L, Pinna S, Huang D, Gustafsson MV, Karinou F, Casula GA, Shoji Y, Takamura Y, Mizumoto T, Soltani M. An integrated magneto-optic modulator for cryogenic applications. *Nature Electronics*. 2022 Sep;5(9):604-10.
53. Dong, Mark, Genevieve Clark, Andrew J. Leenheer, Matthew Zimmermann, Daniel Dominguez, Adrian J. Menssen, David Heim, Gerald Gilbert, Dirk Englund, and Matt Eichenfield. "High-speed programmable photonic circuits in a cryogenically compatible, visible–near-infrared 200 nm CMOS architecture." *Nature Photonics* 16, no. 1 (2022): 59-65.
54. Dong, Mark, David Heim, Alex Witte, Genevieve Clark, Andrew J. Leenheer, Daniel Dominguez, Matthew Zimmermann et al. "Piezo-optomechanical cantilever modulators for VLSI visible photonics." *APL Photonics* 7, no. 5 (2022).
55. Feng, Lantian, Ming Zhang, Jianwei Wang, Xiaoqi Zhou, Xiaogang Qiang, Guangcan Guo, and Xifeng Ren. "Silicon photonic devices for scalable quantum information applications." *Photonics Research* 10, no. 10 (2022): A135-A153.
56. Hogle, Craig W., Daniel Dominguez, Mark Dong, Andrew Leenheer, Hayden J. McGuinness, Brandon P. Ruzic, Matt Eichenfield, and Daniel Stick. "High-fidelity trapped-ion qubit operations with scalable photonic modulators." *npj Quantum Information* 9, no. 1 (2023): 74.
57. Evered, Simon J., Dolev Bluvstein, Marcin Kalinowski, Sepehr Ebadi, Tom Manovitz, Hengyun Zhou, Sophie H. Li et al. "High-fidelity parallel entangling gates on a neutral-atom quantum computer." *Nature* 622, no. 7982 (2023): 268-272.
58. Olsson, Roy H., et al. "Post-CMOS-compatible aluminum nitride resonant MEMS accelerometers." *Journal of Microelectromechanical Systems* 18.3 (2009): 671-678.
59. Wojciechowski, Kenneth E., et al. "A fully integrated oven controlled microelectromechanical oscillator—Part I: Design and fabrication." *Journal of Microelectromechanical Systems* 24.6 (2015): 1782-1794.
60. Crawley, Edward F., and Javier De Luis. "Use of piezoelectric actuators as elements of intelligent structures." *AIAA journal* 25, no. 10 (1987): 1373-1385.



61. Benjeddou, Ayech, Marcelo A. Trindade, and Roger Ohayon. "A unified beam finite element model for extension and shear piezoelectric actuation mechanisms." *Journal of Intelligent Material Systems and Structures* 8, no. 12 (1997): 1012-1025.
62. Chen, Chin-Lin. *Foundations for guided-wave optics*. John Wiley & Sons, 2006.
63. Davis, T. A., and K. Vedam. "Photoelastic Properties of Sapphire ( $\alpha$ -Al<sub>2</sub>O<sub>3</sub>)." *Journal of Applied Physics* 38, no. 11 (1967): 4555-4556.
64. Donadio, D., M. Bernasconi, and F. Tassone. "Photoelasticity of crystalline and amorphous silica from first principles." *Physical Review B* 68, no. 13 (2003): 134202
65. Wiederhecker, Gustavo S., Paulo Dainese, and Thiago P. Mayer Alegre. "Brillouin optomechanics in nanophotonic structures." *APL photonics* 4.7 (2019).
66. Arosa, Yago, and Raúl de la Fuente. "Refractive index spectroscopy and material dispersion in fused silica glass." *Optics Letters* 45, no. 15 (2020): 4268-4271.
67. Singh, Kevin, Shraddha Anand, Andrew Pocklington, Jordan T. Kemp, and Hannes Bernien. "Dual-element, two-dimensional atom array with continuous-mode operation." *Physical Review X* 12, no. 1 (2022): 011040.
68. Zeng, Yong, Peng Xu, Xiaodong He, Yangyang Liu, Min Liu, Jin Wang, D. J. Papoular, G. V. Shlyapnikov, and Mingsheng Zhan. "Entangling two individual atoms of different isotopes via Rydberg blockade." *Physical Review Letters* 119, no. 16 (2017): 160502.
69. Bruzewicz, Colin D., John Chiaverini, Robert McConnell, and Jeremy M. Sage. "Trapped-ion quantum computing: Progress and challenges." *Applied Physics Reviews* 6, no. 2 (2019).
70. Inlek, Ismail Volkan, Clayton Crocker, Martin Lichtman, Ksenia Sosnova, and Christopher Monroe. "Multispecies trapped-ion node for quantum networking." *Physical review letters* 118, no. 25 (2017): 250502.
71. Bagratashvili, Victor N., Svetlana I. Tsympina, Victor A. Radtsig, Aleksey O. Rybaltovskii, Pavel V. Chernov, Sergey S. Alimpiev, and Yaroslav O. Simanovskii. "Inhomogeneous nature of UV absorption bands of bulk and surface oxygen-deficient centers in silica glasses." *Journal of non-crystalline solids* 180, no. 2-3 (1995): 221-229.
72. Thielsch, R., A. Gatto, J. Heber, and N. Kaiser. "A comparative study of the UV optical and structural properties of SiO<sub>2</sub>, Al<sub>2</sub>O<sub>3</sub>, and HfO<sub>2</sub> single layers deposited by reactive evaporation, ion-assisted deposition and plasma ion-assisted deposition." *Thin Solid Films* 410, no. 1-2 (2002): 86-93.
73. Achatz, P., J. A. Garrido, M. Stutzmann, Oliver Aneurin Williams, D. M. Gruen, A. Kromka, and D. Steinmüller. "Optical properties of nanocrystalline diamond thin films." *Applied Physics Letters* 88, no. 10 (2006).
74. Orlandi, Piero, Francesco Morichetti, Michael John Strain, Marc Sorel, Andrea Melloni, and Paolo Bassi. "Tunable silicon photonics directional coupler driven by a transverse temperature gradient." *Optics letters* 38, no. 6 (2013): 863-865.
75. Teshigahara, Akihiko, Ken-ya Hashimoto, and Morito Akiyama. "Scandium aluminum nitride: Highly piezoelectric thin film for RF SAW devices in multi GHz range." *2012 IEEE International Ultrasonics Symposium*. IEEE, 2012.

76. Verma, Anjneya, et al. "Interdependence of piezoelectric coefficient and film thickness in LiTaO<sub>3</sub> cantilevers." *Journal of the American Ceramic Society* 104.5 (2021): 1966-1977
77. Molesky, Sean, Zin Lin, Alexander Y. Piggott, Weiliang Jin, Jelena Vucković, and Alejandro W. Rodriguez. "Inverse design in nanophotonics." *Nature Photonics* 12, no. 11 (2018): 659-670.
78. Lin, Zin, Marko Lončar, and Alejandro W. Rodriguez. "Topology optimization of multi-track ring resonators and 2D microcavities for nonlinear frequency conversion." *Optics letters* 42.14 (2017): 2818-2821.
79. Golter, D. Andrew, Genevieve Clark, Tareq El Dandachi, Stefan Krastanov, Andrew J. Leenheer, Noel H. Wan, Hamza Raniwala et al. "Selective and scalable control of spin quantum memories in a photonic circuit." *Nano Letters* 23, no. 17 (2023): 7852-7858.
80. Clark, Genevieve, Hamza Raniwala, Matthew Koppa, Kevin Chen, Andrew Leenheer, Matthew Zimmermann, Mark Dong et al. "Nanoelectromechanical Control of Spin-Photon Interfaces in a Hybrid Quantum System on Chip." *Nano Letters* 24, no. 4 (2024): 1316-1323
81. Estevez, M.C., Alvarez, M. and Lechuga, L.M., 2012. Integrated optical devices for lab-on-a-chip biosensing applications. *Laser & Photonics Reviews*, 6(4), pp.463-487
82. Stanfield, P. R., A. J. Leenheer, C. P. Michael, R. Sims, and M. Eichenfield. "CMOS-compatible, piezo-optomechanically tunable photonics for visible wavelengths and cryogenic temperatures." *Optics express* 27, no. 20 (2019): 28588-28605
83. Inoue, Yuki, Tomotake Matsumura, Masashi Hazumi, Adrian T. Lee, Takahiro Okamura, Aritoki Suzuki, Takayuki Tomaru, and Hiroshi Yamaguchi. "Cryogenic infrared filter made of alumina for use at millimeter wavelength." *Applied optics* 53, no. 9 (2014): 1727-1733
84. Sakaguri, Kana, Masaya Hasegawa, Yuki Sakurai, Junna Sugiyama, Nicole Farias, Charles A. Hill, Bradley R. Johnson et al. "Anti-reflection coating with mullite and Duroid for large-diameter cryogenic sapphire and alumina optics." *Applied Optics* 63, no. 6 (2024): 1618-1627.
85. Storz, R., C. Braxmaier, K. Jäck, O. Pradl, and S. Schiller. "Ultrahigh long-term dimensional stability of a sapphire cryogenic optical resonator." *Optics letters* 23, no. 13 (1998): 1031-1033.
86. Seel, Stefan, Rafael Storz, Giuseppe Ruoso, Jürgen Mlynek, and Stephan Schiller. "Cryogenic optical resonators: a new tool for laser frequency stabilization at the 1 Hz level." *Physical review letters* 78, no. 25 (1997): 4741
87. McKenna, Timothy P., Jeremy D. Witmer, Rishi N. Patel, Wentao Jiang, Raphaël Van Laer, Patricio Arrangoiz-Arriola, E. Alex Wollack, Jason F. Herrmann, and Amir H. Safavi-Naeini. "Cryogenic microwave-to-optical conversion using a triply resonant lithium-niobate-on-sapphire transducer." *Optica* 7, no. 12 (2020): 1737-1745.
88. Verhoeve, P. "UV/optical imaging spectroscopy with cryogenic detectors." *Nuclear Instruments and Methods in Physics Research Section A: Accelerators, Spectrometers, Detectors and Associated Equipment* 444, no. 1-2 (2000): 435-440

Supplemental

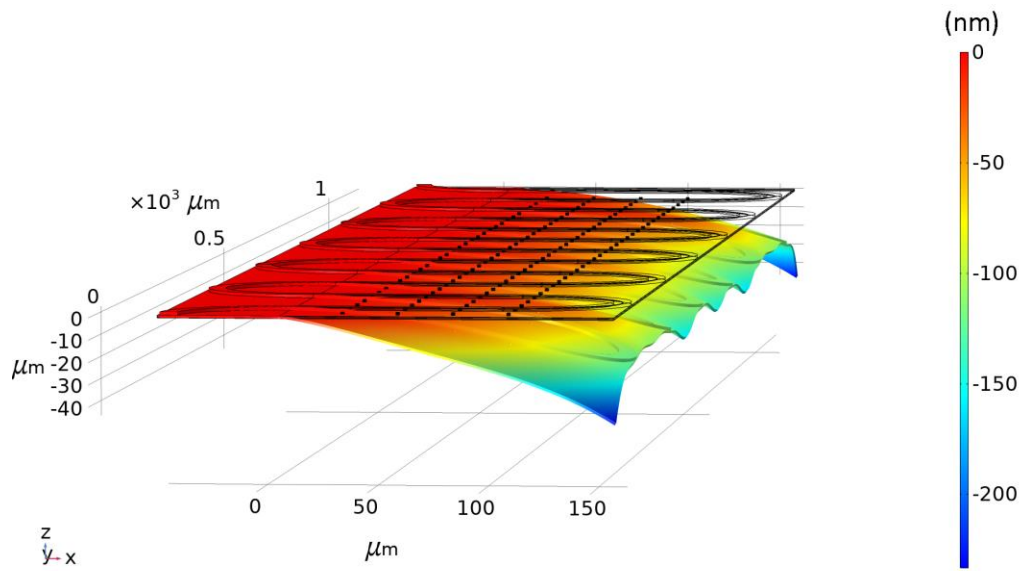


Figure S1. COMSOL Multiphysics simulations of CMZI mechanical deflection for 20 V applied voltage.

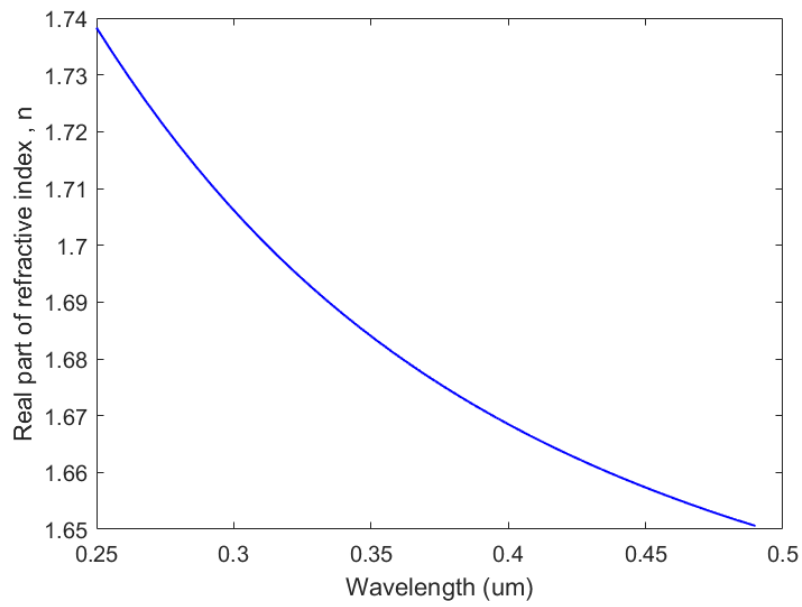


Figure S2. Real part of alumina refractive index used for modeling.

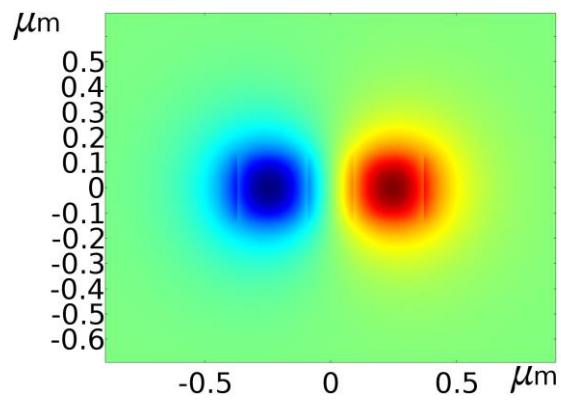


Figure S3. Coupler asymmetric TE mode  $E_y$  field distribution and geometry.

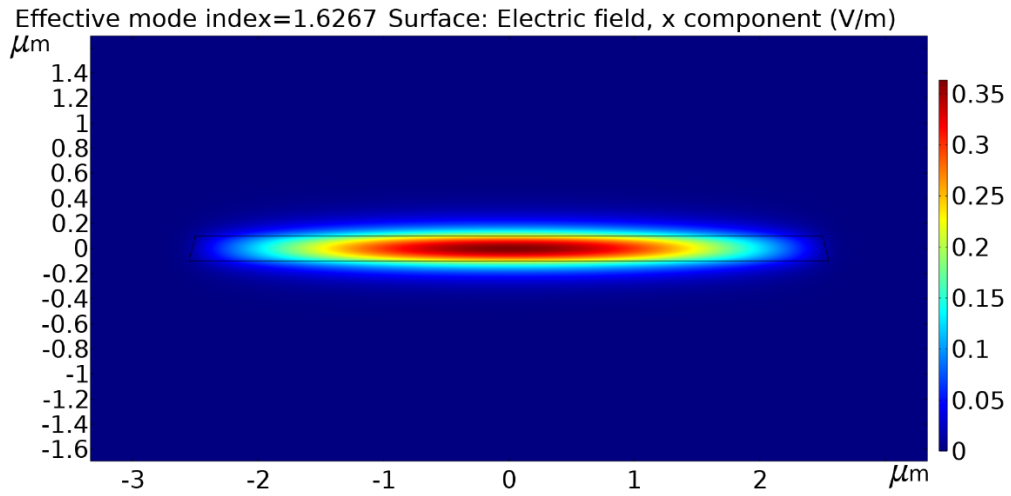


Figure S4. Racetrack resonator waveguide TE mode profile.

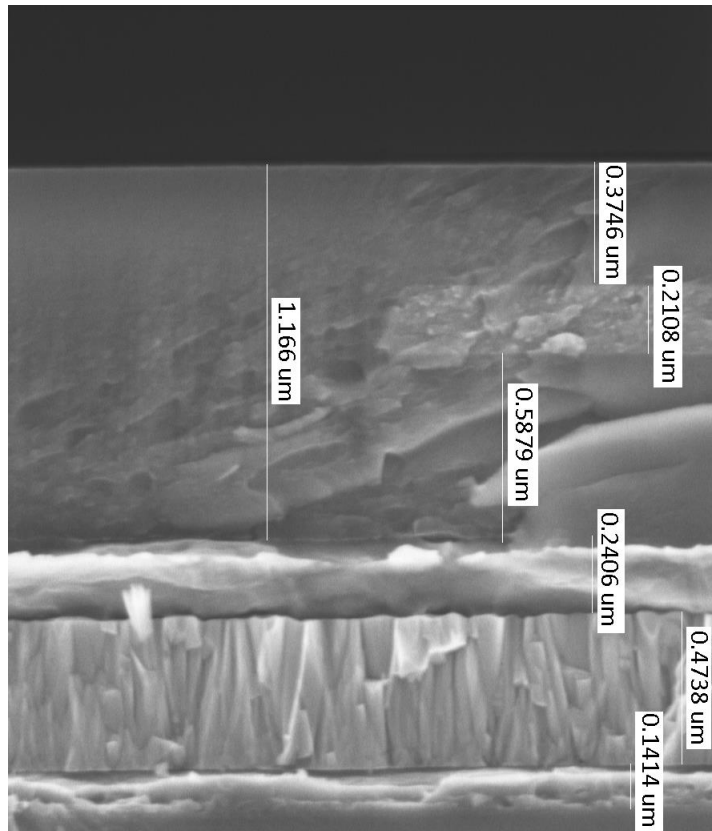


Figure S5. SEM cross-section of the fabricated racetrack resonator device with layer dimensions.

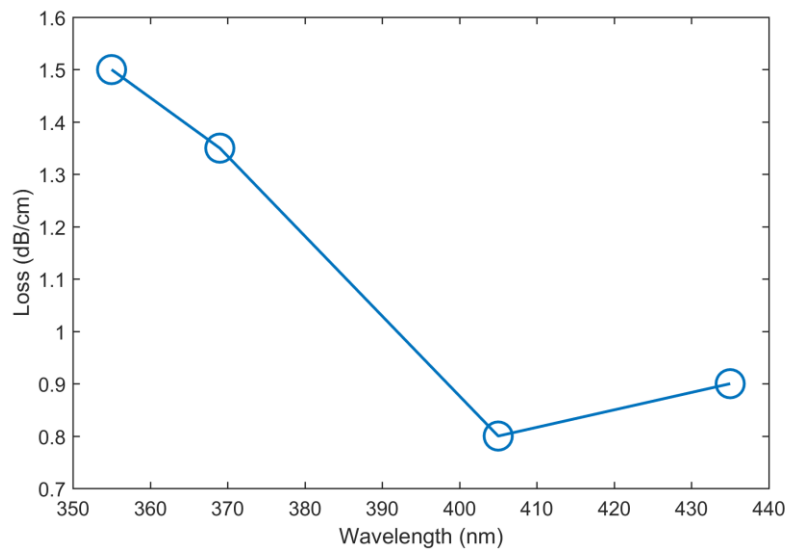


Figure S5. Alumina waveguide losses vs wavelength